Journal of ASTM International, Vol. 7, No. 2
Paper ID JAI102529
Available online at www.astm.org

Nathan A. Branch,[1] *Nagaraj K. Arakere,*[1] *Vaughn Svendsen,*[2] *and Nelson H. Forster*[2]

Stress Field Evolution in a Ball Bearing Raceway Fatigue Spall

ABSTRACT: The governing mechanisms of fatigue spall propagation in ball bearing inner raceways are investigated through the use of elastic-plastic finite element modeling, X-ray diffraction, and the visual inspection of fatigue spall cracks. The model simulates multiple ball impacts with a fatigue spall's edge in a 208 size ball bearing operating at 10,000 rpm. Ball impacts are shown to cause severe plastic deformation within the spall edge and induce tensile residual stresses. The finite element results are supported by X-ray diffraction measurements and the locations of cracks observed around the edge of a spall.

KEYWORDS: rolling element bearings, rolling contact fatigue, spall propagation, contact mechanics, bearing steels, gas/jet turbines, impact wear, elastic-plastic finite element analysis, residual stresses, X-ray diffraction

Introduction

The ever increasing demand for safer and more efficient military and commercial jet aircraft engines has encouraged the design of high performance bearings that have better corrosion resistance, longer rolling contact fatigue (RCF) life, and higher thrust load capacity. Hybrid bearings that use silicon nitride balls and case hardened metal raceways can meet these demands and substantially out-perform conventional through-hardened steel bearings [1–3].

However, even high performance bearings are not immune from the deleterious effects caused by improper lubrication, foreign object debris, and excessive loading, all of which can cause surface fatigue failure [4]. These surface fatigue failures occur in the form of surface pitting or spalls on a ball or raceway surface. This type of surface fatigue failure is also observed in gears, cam-followers, and rails [5,6].

Conventional bearing fatigue life is usually defined as the amount of time or number of load cycles needed to initiate a surface spall. Impending bearing failure from RCF cannot be accurately predicted or detected until the bearing has started to liberate material in the form of fatigue spalls. Thus, the period of time from spall initiation to total failure becomes quite important. More robust materials with a high resistance to fatigue crack initiation and low spall propagation rate would help extend the period of detection and improve engine reliability.

Past and Current Research

Understanding the effects of plasticity, contact stress, fatigue, material microstructure, rate dependency, and residual stress formation in the vicinity of a spall is essential to designing safer bearings. However research of the governing mechanisms of spall propagation is limited. Probabilistic bearing life prediction models that are based on equations developed by Lundberg and Palmgren [7] are often used to estimate the life of a spalled bearing but neglect important effects such as localized plasticity. A comprehensive review and comparison of these bearing life theories are presented by Zaretsky et al. [8] and Sadeghi et al. [4]. Kotzalas and Harris [9] studied spall progression on chemical vapor deposition (CVD) American Iron and Steel Institute (AISI) 52100 steel balls that were driven by vacuum induction melted, vacuum arc remelted (VIM VAR) M50 steel V-Ring raceways and extended the bearing life prediction methods of Ioannides and

Manuscript received May 17, 2009; accepted for publication October 23, 2009; published online December 2009.
[1] Mechanical and Aerospace Engineering, Univ. of Florida, Gainesville, FL 32611 (Corresponding author), e-mail: nagaraj@ufl.edu
[2] Propulsion Directorate, Air Force Research Laboratory, Wright Patterson Air Force Base, OH 45433.

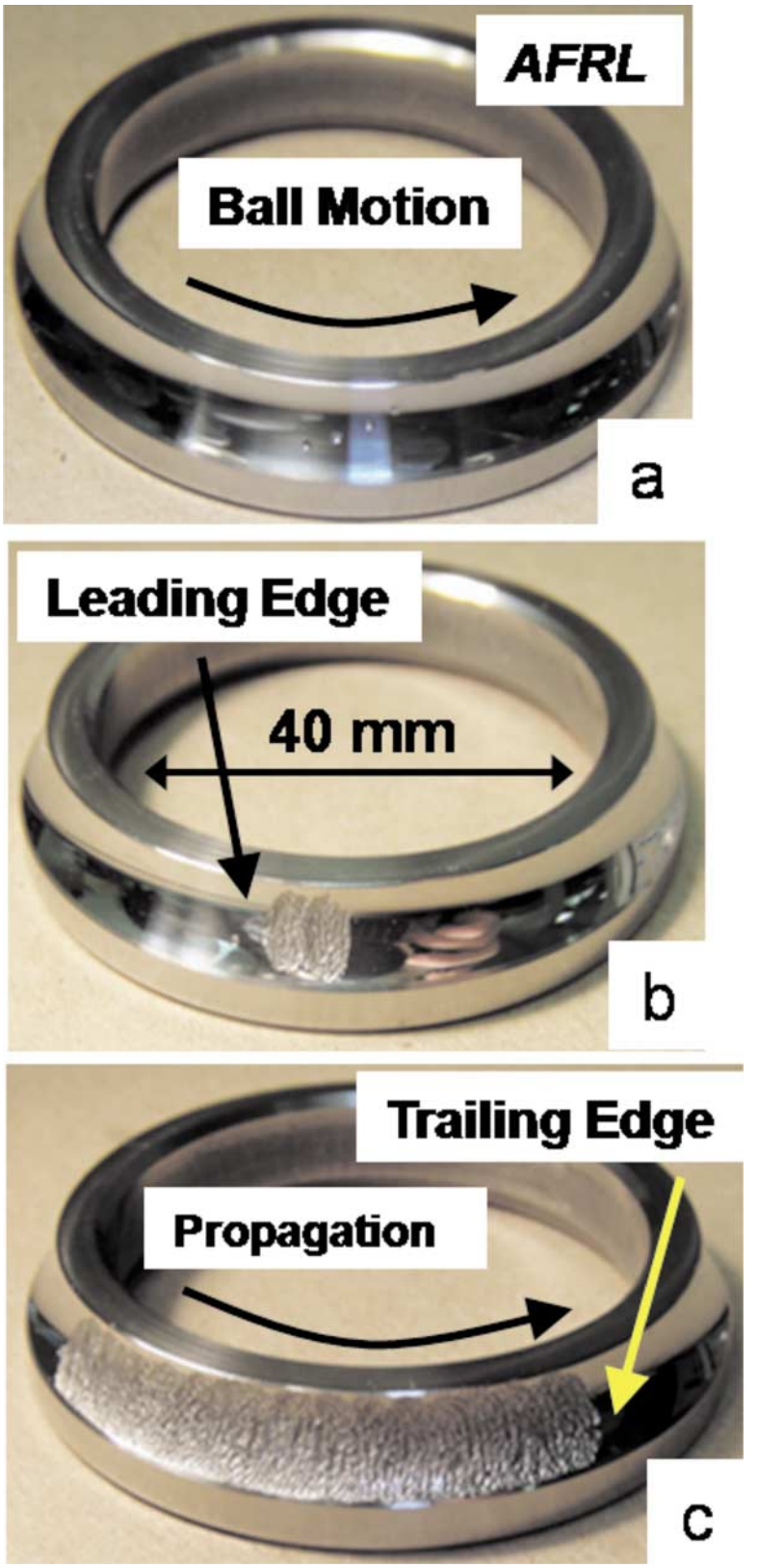

FIG. 1—*(a) Virgin raceway. (b) Small spall. (c) Progressed spall.*

Harris [10] to predict the remaining useful life of spalled bearings. Xu and Sadeghi [11] implemented damage accumulation laws within representative volume elements undergoing RCF to model the transformation of a dent into a progressed spall.

The spall propagation experiments on tapered roller bearings by Hoeprich [12] highlighted the randomness inherent to spall propagation and its unknown governing mechanisms. In a recent three-part

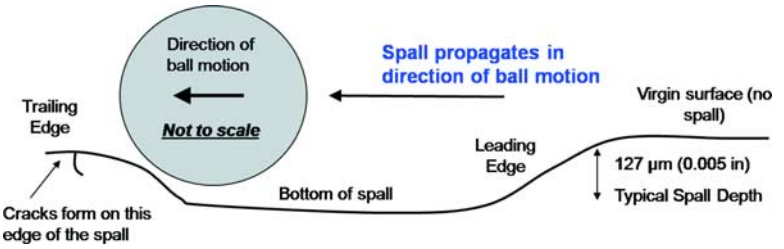

FIG. 2—*Ball impact with spall's edge influences propagation direction.*

series, an experimental and numerical investigation of spall propagation was presented [13–15]. Part I by Rosado et al. [13] showed the dependency of spall propagation rate on material selection and contact stress. Part II by Arakere et al. [14] presented the static elastic-plastic stress fields around an initial fatigue spall, the likely conditions that contribute to initial spall growth, and the importance of including plasticity effects in bearing fatigue life calculations. Part III by Forster et al. [15] investigated the effects of alloy

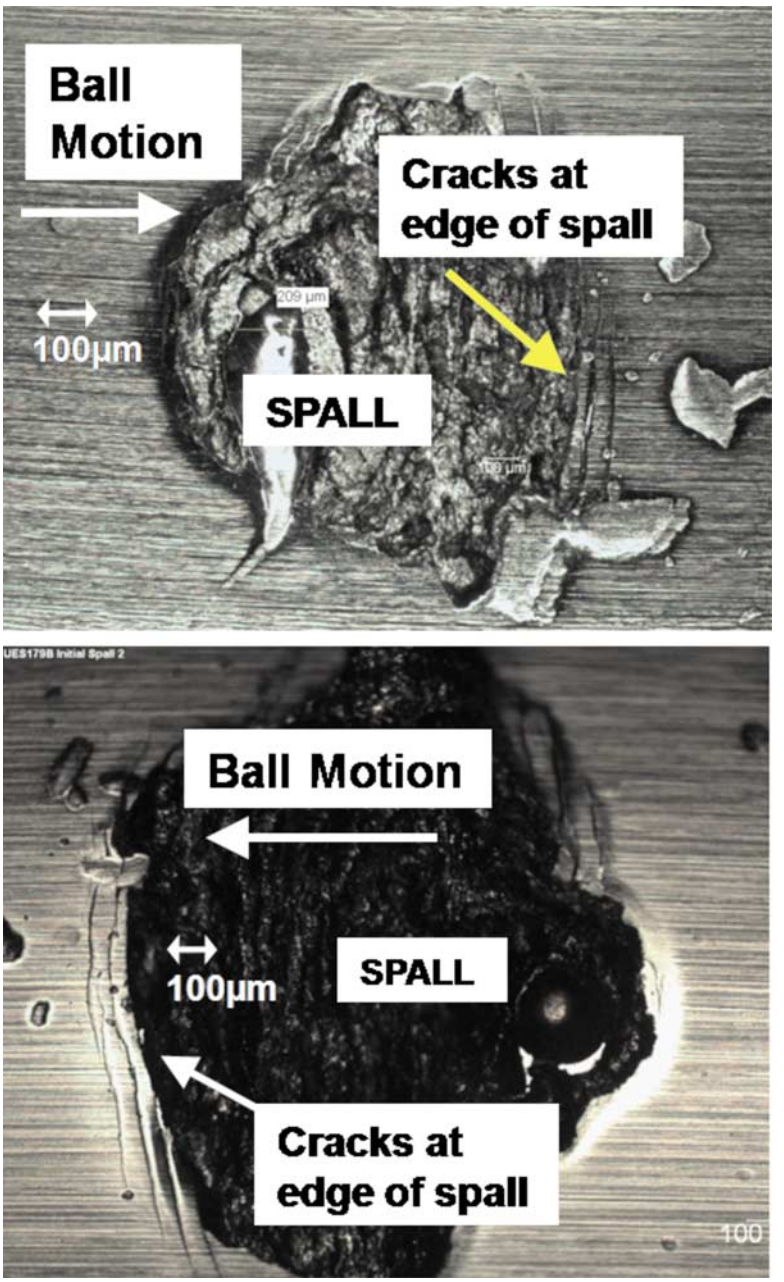

FIG. 3—*Two examples of cracks on trailing edge of propagating spall.*

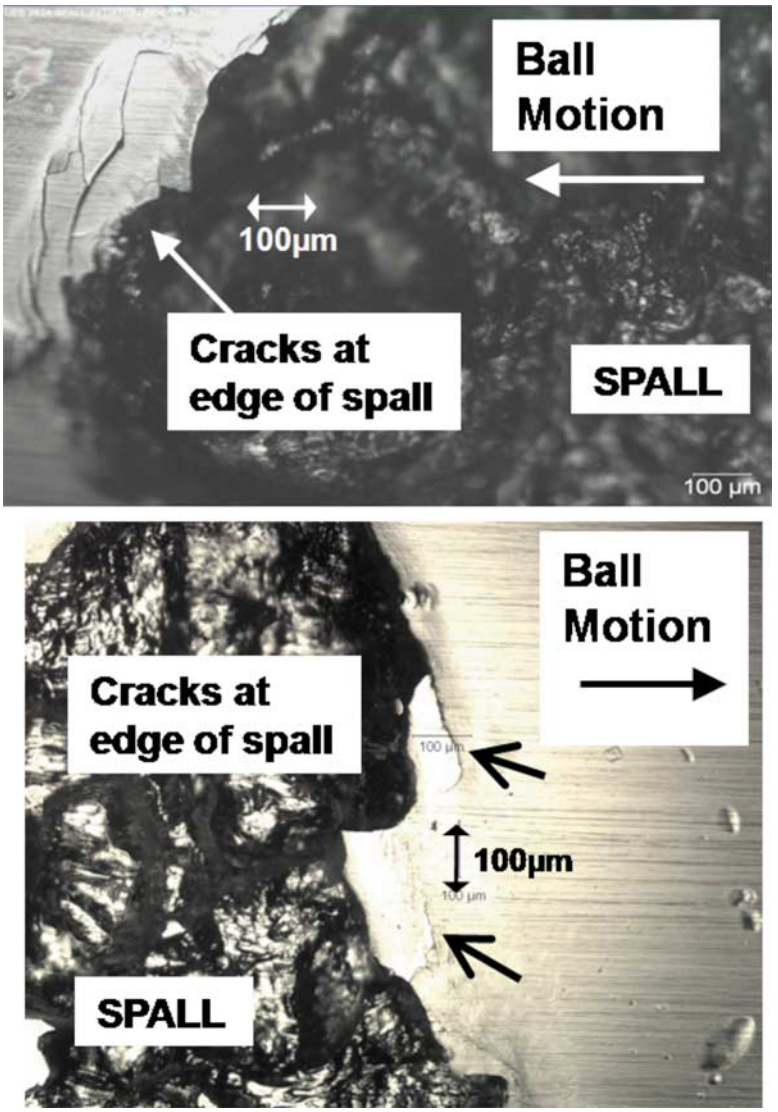

FIG. 4—*Two examples of close up images of spall's edge cracks.*

content, heat treatment, and residual stresses on the stability of the microstructure and alterations in residual stress profile ultimately impacting bearing fatigue life and propagation rate.

The analysis presented here is unique because it uses finite element models that include the effects of plasticity to calculate the critical stresses and strains that develop within a spall edge during and after successive ball impacts. The results are supported by the residual stresses calculated by X-ray diffraction (XRD) techniques and the location of cracks on an impacted spall edge. This information will support a plausible scenario of why fatigue spalls propagate. This analysis represents a first step toward identifying how material properties, bearing geometry, and operating conditions contribute to spall propagation and eventual bearing failure.

Nature of Spall Propagation

Spalls propagate predominately in the direction of ball motion during surface fatigue failure in bearings [12,13]. Figure 1 shows an example of damage progression along a bearing inner raceway. In the experiments explained in Ref 13, spalls are initiated naturally from material fatigue or by Rockwell C indentations, which act as stress risers and accelerate the spall initiation process. During bearing operation cracks develop around the indent, liberate surface material, and form a small initial spall. The initial spall will widen during operation as described in Ref 14 and eventually allow the ball to descend into the spall and impact the trailing edge. The spall will then progress around the raceway in the direction of ball motion

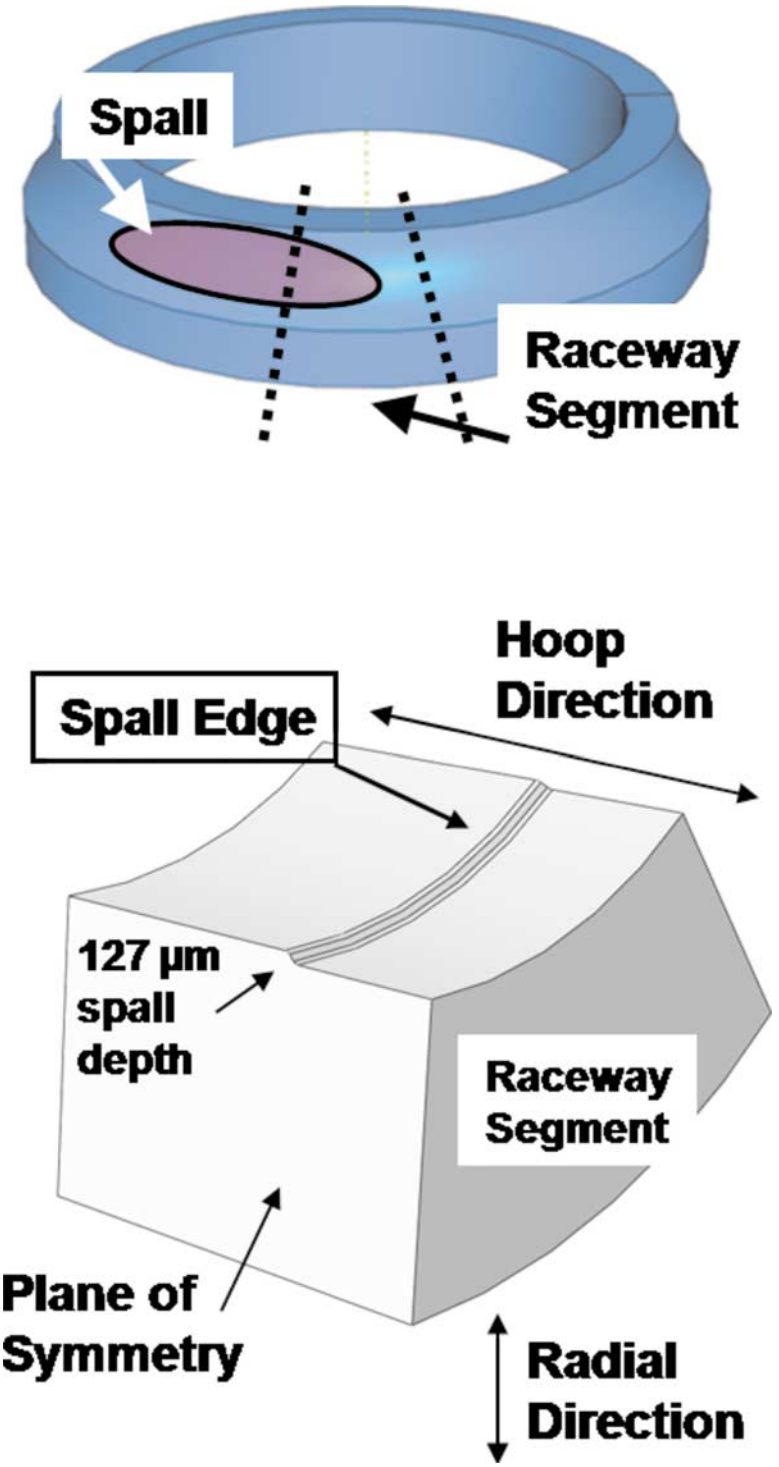

FIG. 5—*Finite element model geometry.*

until catastrophic failure occurs (Fig. 1(*c*)). Usually the catastrophic failure mode is fracture of the bearing cage leading to bearing seizure.

The spall's trailing edge will be defined as the edge that deteriorates with continuous bearing operation, whereas the spall's leading edge is a portion of the initial spall and does not liberate significant material during operation.

The numerous impacts that occur between balls and the trailing edge of the spall are believed to be the main driving forces of spall propagation (Fig. 2). The trailing edge is the only spall edge that is subjected to ball impacts *and* deteriorating; clearly there is a relationship between the two.

Also, significant cracks form only on the spall's trailing edge (Figs. 3 and 4) as the spall is propagat-

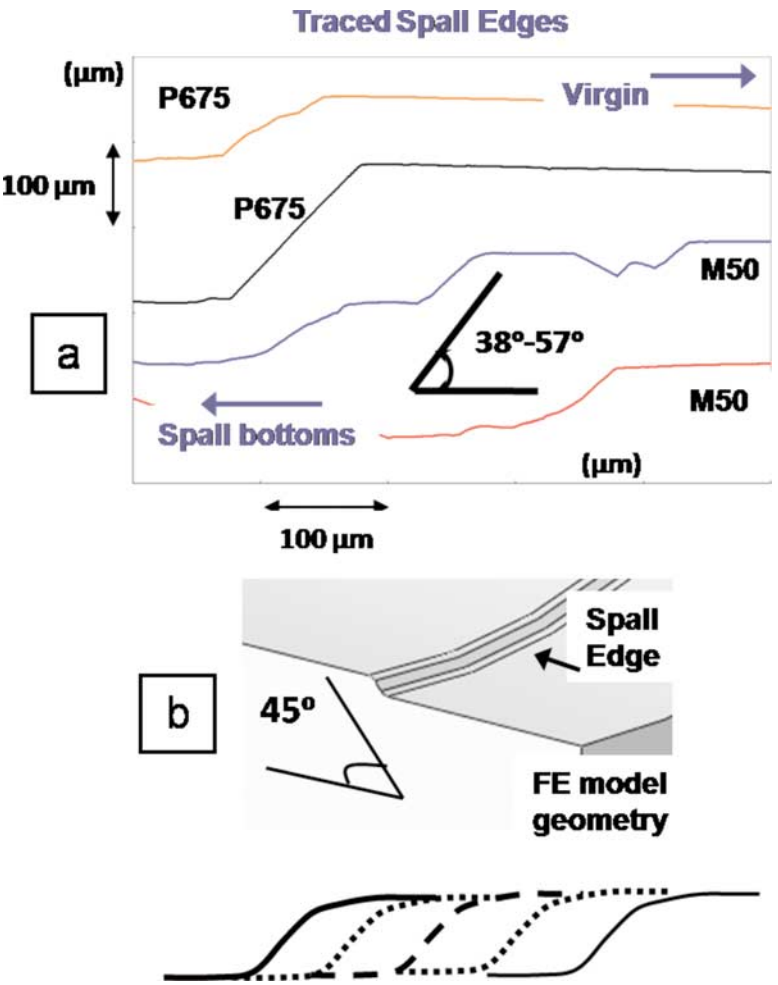

FIG. 6—*(a) Tracings of spall edges from M50 and Pyrowear 675 bearing steels. (b) Consistent spall edge during propagation and used in FE model.*

ing. This is another indication that more damage is occurring on the impacted edge in the form of cracks and not on the leading edge. Continuous ball impacts are believed to encourage these edge cracks to grow and cause fragments of material to liberate from the raceway's surface. The fragments collected by the Oil Debris Monitor in [13] were typically the same size as the edge of the spall.

This continuous loss of surface material increases the clearance between the bearing's inner and outer raceways, which creates enough space for the engine shaft to misalign. Severe vibrations, heat, noise, and eventual catastrophic bearing failure are then likely to occur.

Procedure and Finite Element Model

The finite element model must capture the geometry and physics of bearing operation as accurately as possible. However, this analysis will not model the entire inner and outer rings, all balls, lubrication, temperature effects, and interactions with the bearing cage. For this purpose, only a segment of the inner ring will be modeled in the interest of computational efficiency (Fig. 5). The raceway segment will include the trailing edge of the spall since we are investigating the types of damage this specific spall edge is likely to develop during ball impact.

To best capture the geometry of the spall's edge, profilometer tracings were taken of the spall's trailing edge on four different raceways made of Pyrowear 675 (P675) case hardened and M50 through-hardened bearing steels (Fig. 6(*a*)). An average spall edge slope of 45° is determined from the four profile measurements and is applied to the finite element (FE) model geometry (Fig. 6(*b*)). This edge geometry is constant during spall propagation (Fig. 6(*b*)) and suggests that the failure mode controlling material loss from the spall's edge is the same regardless of spall length.

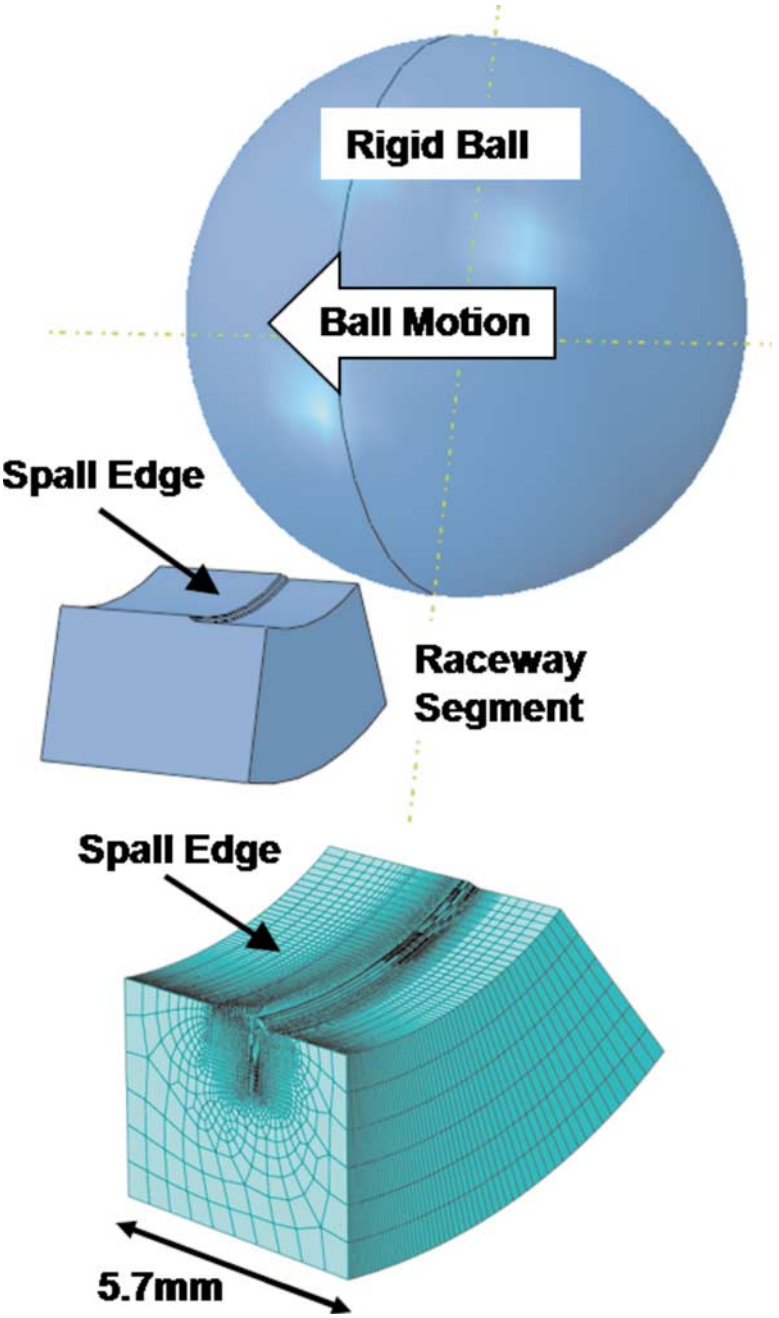

FIG. 7—*FE model of ball impacting spall edge and finite element mesh.*

The finite element model will simulate three successive rigid ball impacts on the same spall edge at a ball velocity of 15.24 m/s (50 ft/s) (Fig. 7). The ball velocity is determined from the known rotational speeds of the cage and inner raceway of the 40 mm bearing used in Refs 13–15. Three impacts were chosen because there was no significant change in the stresses and strains within the spall edge after the second and third impacts.

Rigid balls do not require a mesh and reduce the number of elements in the model. All three of the balls have the density of steel (8 g/cm^3) and are expected to impart more energy into the spall than compared to a silicon nitride ball. The ball is not allowed to spin and can only translate within the plane of symmetry. Since contact is frictionless, the rotational kinetic energy of the ball will not significantly affect the nature of impact between ball and spall edge.

In house compression tests were performed on M50 steel specimens (Fig. 8) to obtain its stress strain curve up to 0.013 plastic strain and compared well with data available from Carpenter [16]. Since the plastic behavior of this material after 1.3 % plastic strain is unknown or unobtainable from other sources, the material is assumed to behave in a perfectly plastic manner after this strain is reached. Typically, very

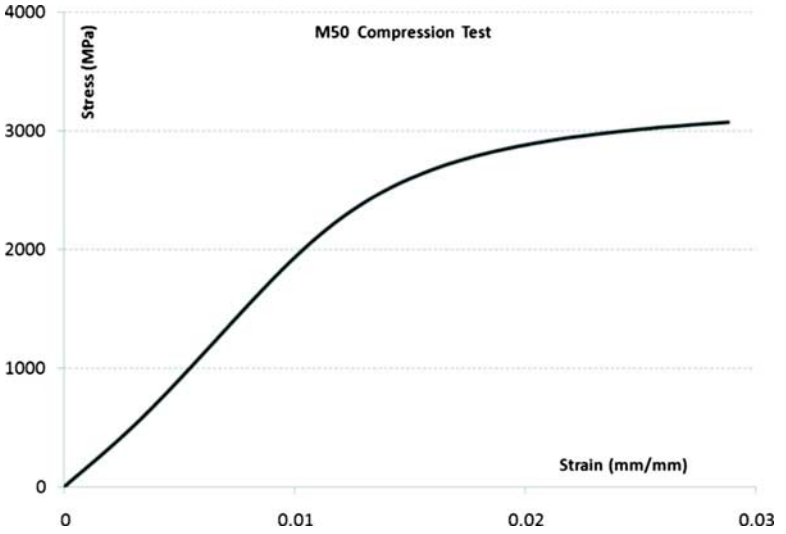

FIG. 8—*Flow curve, M50 steel.*

hard materials do not have a capacity to strain harden like copper or 303 stainless steel, so a perfectly plastic response is a reasonable assumption for this bearing steel and this analysis.

A very fine linear hexahedral mesh is designed around the spall's edge because the most critical stresses and strains are forming within this small region (Fig. 7). The Explicit solver within ABAQUS v6.8-2 was used since this is a transient analysis and has time dependent properties (the velocity of the ball) [17]. The von Mises (J2) failure criterion, associative flow rule, and isotropic hardening are appropriate for bearing steels and implemented here.

Results and Discussion

All plots of the finite element model results will be close up images of a spall edge's cross section (Fig. 9). The radial and hoop stresses within the spall *during* impact were calculated (Fig. 9) and are mostly compressive as expected. The maximum contact pressure between a ball and spall edge can reach 7 GPa, which is sufficient to cause subsurface yielding. Classical Hertzian contact solutions do not apply here since the spall edge is very sharp and is undergoing considerable deformation during impact.

Of greater interest are the locations and distributions of *residual* tensile stresses around the edge of the spall. It is well understood that tensile residual stresses are detrimental to the fatigue strength of a material because they encourage fatigue crack initiation and growth. The finite element model calculates tensile residual hoop stresses to occur on the surface of the spall's edge after successive ball impacts (Fig. 10). This is significant because this location of residual tensile stress agrees with where cracks are seen around the spall's edge in the bearings from Refs 13 and 15 (Figs. 3 and 4).

The locations and magnitudes of residual hoop stresses within the spall's edge from the FE results are shown in Figs. 10 and 11. Locations D and E best capture the residual tensile stress at the surface mentioned earlier and the residual compressive stresses just beneath the spall's edge. The severity of the residual stresses decreases going away from the spall's edge as shown in profiles A, B, and C.

Also, locations A, B, and C of the finite elements results match closely to the profiles calculated from XRD techniques (Fig. 12) and described in more detail in Ref 15. The results of Forster et al. [15] showed that the changes in residual stress were cumulative over millions of cycles in AISI 52100, AISI M50, and M50 NiL bearings. XRD was done on bearing raceways that had experienced 10^6–10^{10} stress cycles, whereas the model is only simulating three impacts. Therefore, only qualitative comparisons can be made here.

For example, the residual stress profile in Fig. 12(*a*) [15] is from a spall initiated from surface indents and is quite different from the spall initiated from material fatigue without surface indents (Fig. 12(*b*)). This is not captured in the bearing model and may be a result of microstructure decay [15]. Also, the location of the experimental XRD measurement was about 3.2 mm (0.125 in.) from the edge of the spall in all cases. The spot size of the irradiated area is 1.3×1.3 mm^2.

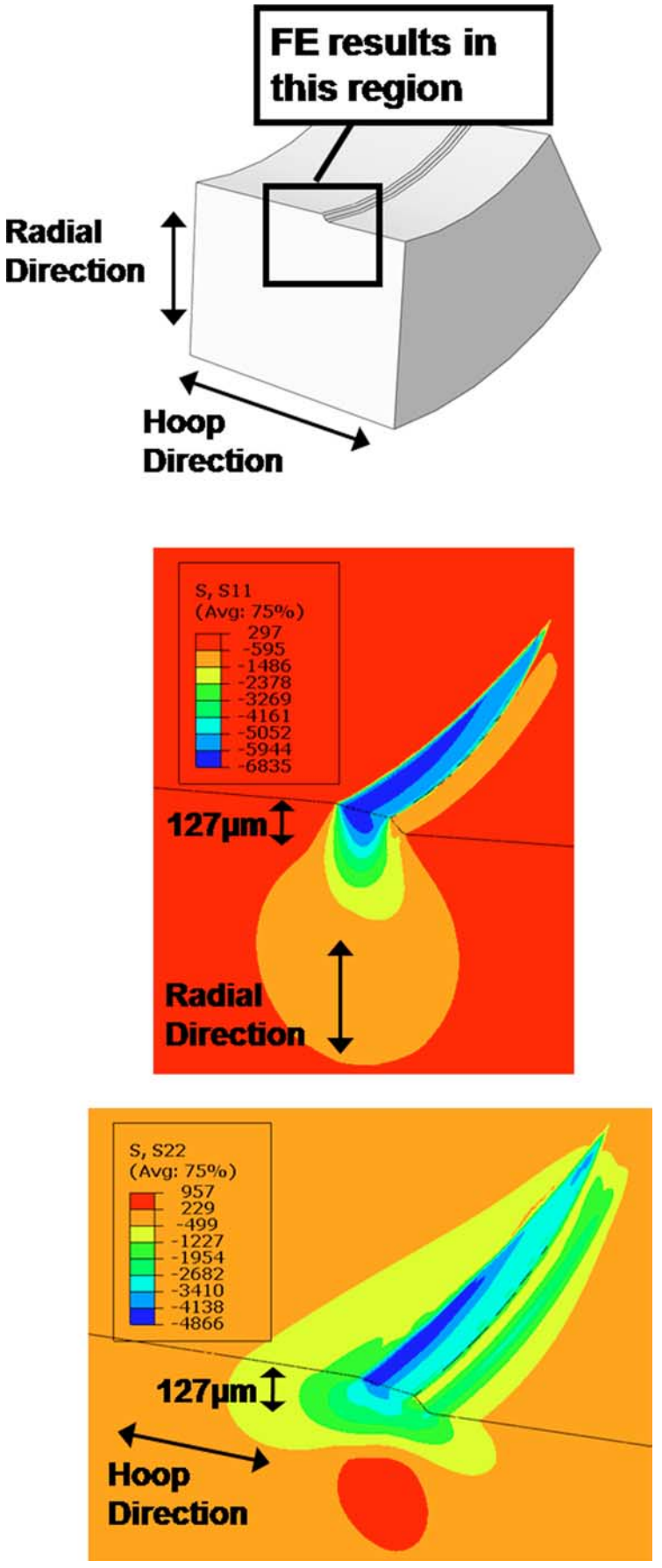

FIG. 9—*Radial and hoop stresses during impact.*

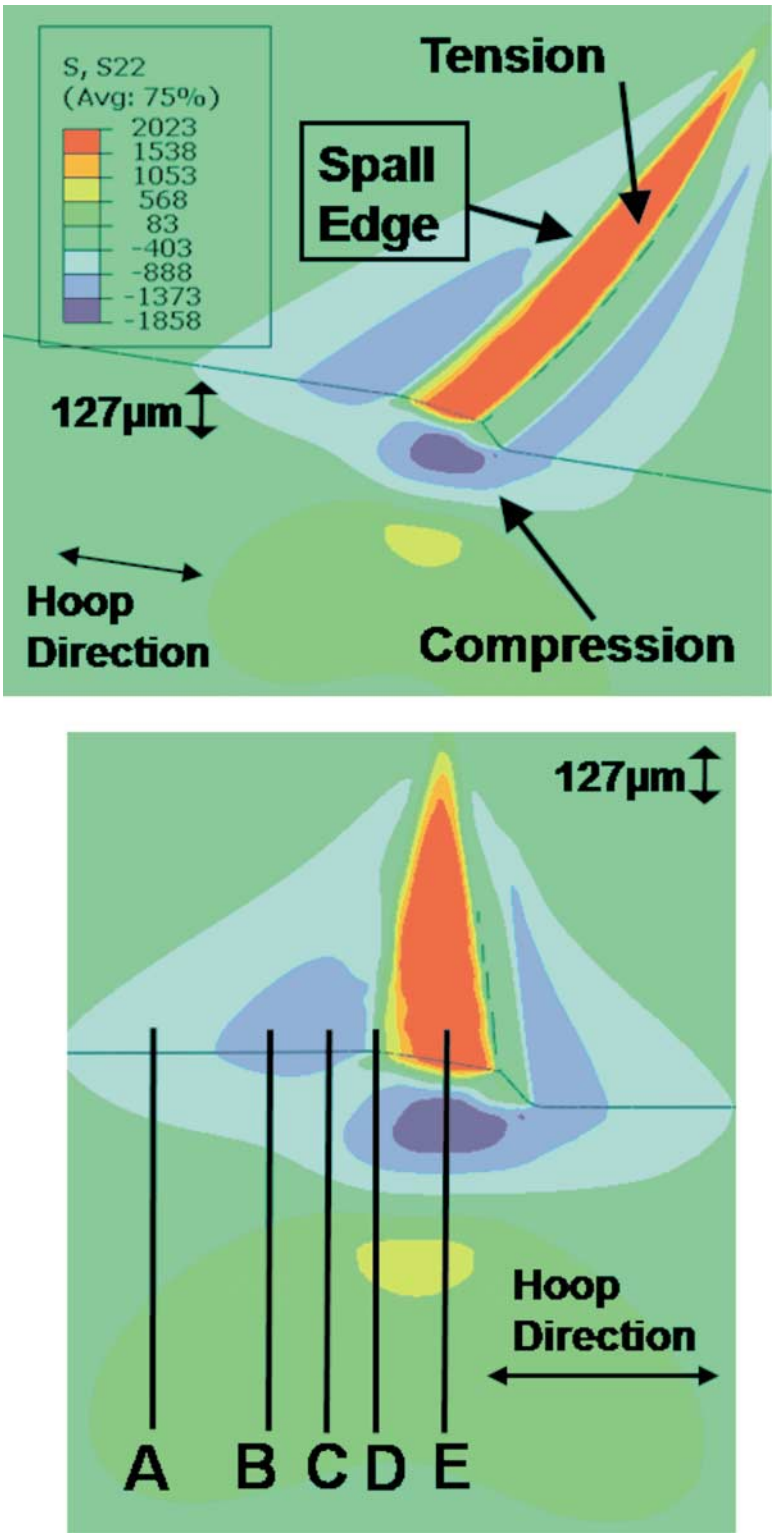

FIG. 10—*(a) Residual stress profile in hoop direction after three impacts. (b) Locations of profiles in Fig. 11.*

The XRD residual stress profiles are not a close match to profiles D and E because the location where XRD was performed was not close enough to the spall's edge to measure the residual tensile stresses shown in profiles D and E. Even if XRD was taken on locations D and E, unknown cracks within the spall's edge could have relieved residual stresses that XRD could not have picked up. This helps explain why the data is not an exact match for every location, but profiles A, B, and C are within the ballpark of what is determined from XRD.

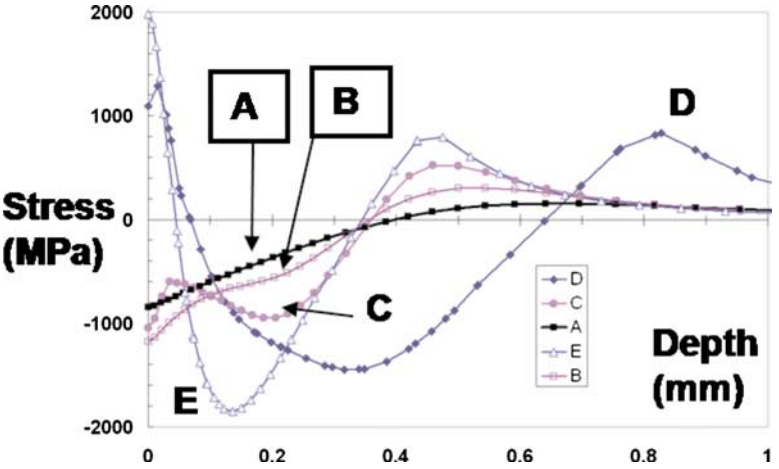

FIG. 11—*Residual hoop stress profiles, finite element results.*

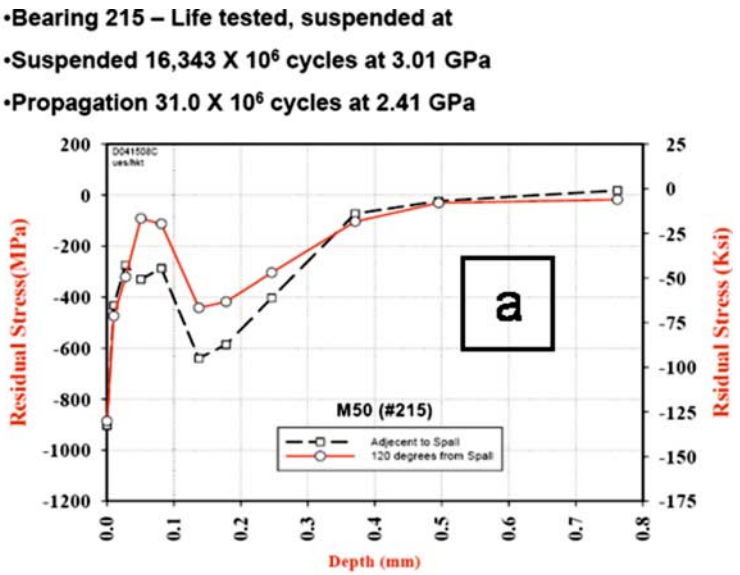

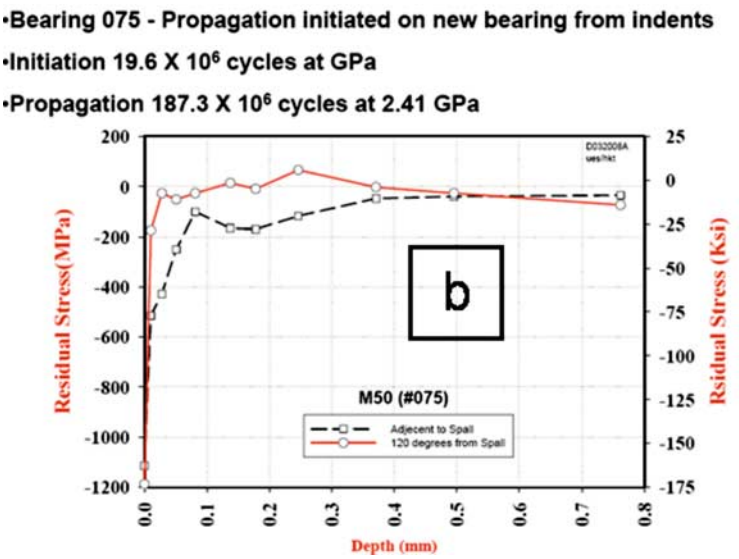

FIG. 12—*XRD residual hoop stress profiles; M50 spalled bearings.*

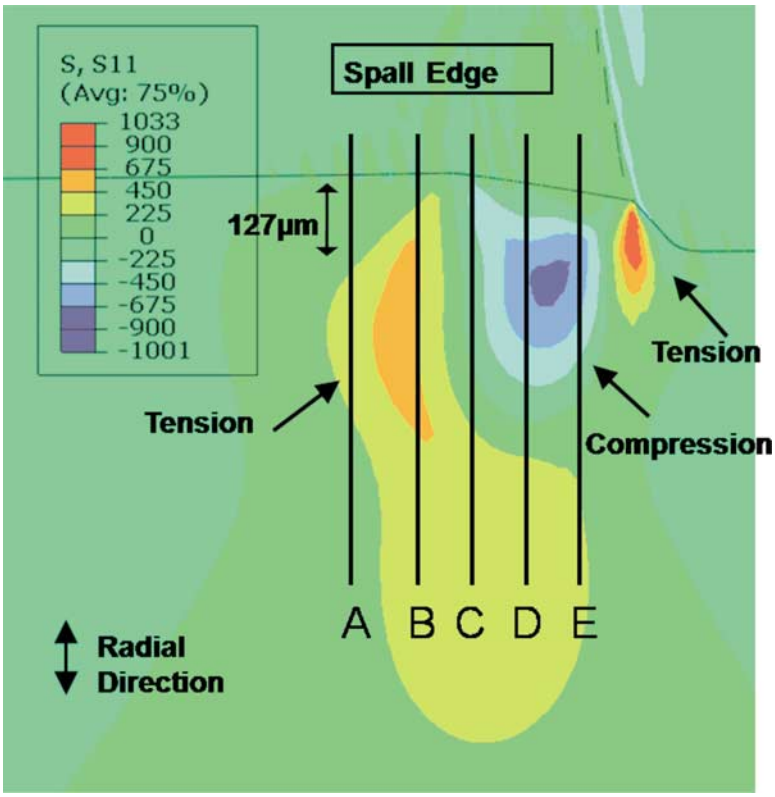

FIG. 13—*Residual stress state in the radial direction and locations of stress profiles shown in Fig. 10.*

Many fatigue failure theories predict tensile *radial* residual stresses to develop in rolling contact [4], which lead to crack formation parallel to the surface. The finite element results show that tensile radial residual stresses exist within the edge of the spall after successive impacts (Fig. 13).

Radial tensile residual stresses encourage fatigue cracks to form and their location matches the spall depth (Figs. 13 and 2). Residual stress profiles are plotted (Fig. 14) at the same locations as the hoop direction plot (Fig. 10). Locations D and E capture the residual compressive stresses just below the spall's edge, while B and C show subsurface residual tensile radial stresses at the same depth as the depth of the spall. The location of residual tensile radial stress explains why the spall depth is consistent throughout spall growth.

The finite element results in Figs. 10 and 13 show compressive residual stresses in both the radial and hoop directions located just below the spall's edge. Compressive residual stresses below the spall's edge

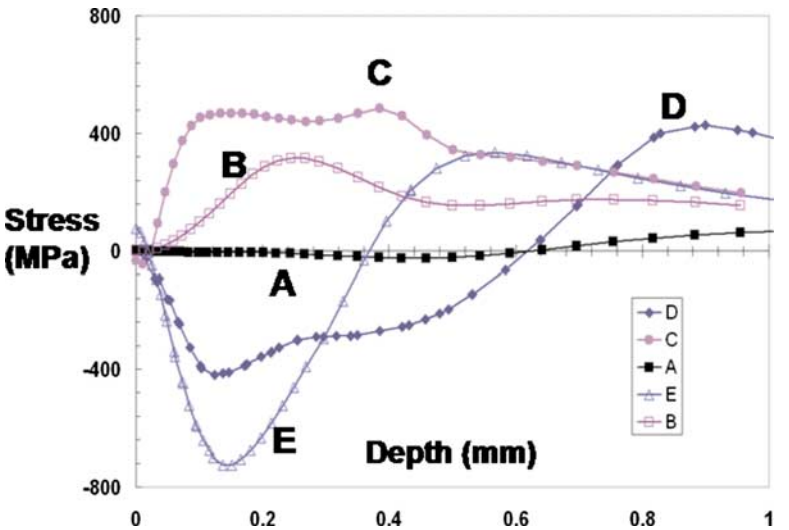

FIG. 14—*Finite element residual stress profiles in radial direction.*

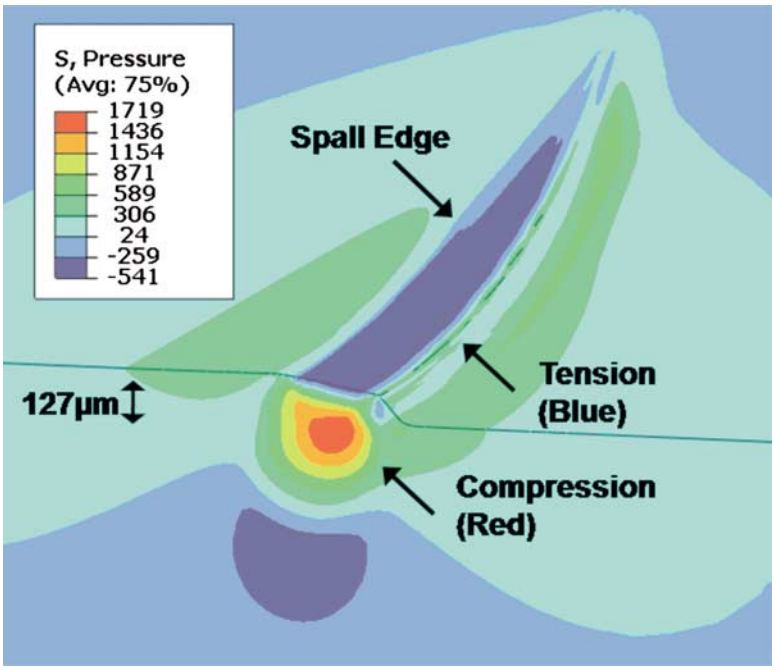

FIG. 15—*Residual hydrostatic stresses.*

retard crack growth [18] and consequently keep material loss localized to the immediate surface. This is observed in experiments and shown in Figs. 2–4.

The location of residual tensile hydrostatic pressure also agrees with where cracks appear in spalled bearings (Figs. 15 and 3). ABAQUS defines tensile hydrostatic pressure as negative, which is why the tensile region is blue instead of red as before. Howell et al. [19] studied rolling contact over a surface indent and showed that cracks are likely to initiate in regions of tensile hydrostatic pressure.

The strain-life approaches summarized in Ref 18, such as Coffin–Manson, have shown that fatigue cracks are likely to initiate in a region of high plastic strain over many load cycles. A detailed quantitative fatigue life analysis cannot be made here since the cyclic strain-life data for bearing steels is scarce, the plastic strains calculated by the FE model are for a spall that has only suffered three impacts, and the cyclic plastic strain amplitudes from the FE model are highly dependent on the cyclic hardening law, which is also limited for bearing steels. However, as a qualitative investigation it is worth comparing the distribution of plastic strain within the spall edge with the location of cracks in the actual bearings to see if cracks form in the most damaged region as predicted by the FE model.

Large amounts of plastic strain in the hoop direction develop on the surface of the spall's edge (Fig. 16) and match closely to where cracks are observed in actual bearing spalls (Figs. 3 and 4). The maximum hoop plastic strain is below the surface and is a likely site of crack initiation.

The distribution of maximum principal plastic strain (Fig. 17) corresponds to the locations of residual tensile hoop stress (Fig. 10), residual radial tensile stress (Fig. 13), residual tensile hydrostatic pressure (Fig. 15), and hoop plastic strain (Fig. 16). Cracks are likely to follow this path of highly damaged material and also aided by the tensile and compressive residual stresses within the spall.

To verify the assumption that cracks follow the path of maximum principal plastic strain, it is shown that the distribution of maximum principal plastic strain (Fig. 17) is also similar to the profilometer tracings of the spall edges (Fig. 6). After a fragment of material is liberated from the spall edge, the new spall edge profile left behind is a close match to the profilometer tracings *and* the distribution of maximum principal plastic strain. This process repeats itself and explains why the spall edge profile does not vary throughout spall propagation.

Spall edge geometry is expected to influence the calculation of stresses and strains in the finite element model; however it can be shown that similar residual stress gradients will develop regardless of spall edge sharpness (Figs. 18 and 19). Two different degrees of spall sharpness were modeled with the same ball velocity and material properties as before. Stress contours of the residual radial stresses within the spall's edge are shown along with a graph of the residual hoop stress profiles. As expected, the stresses around a

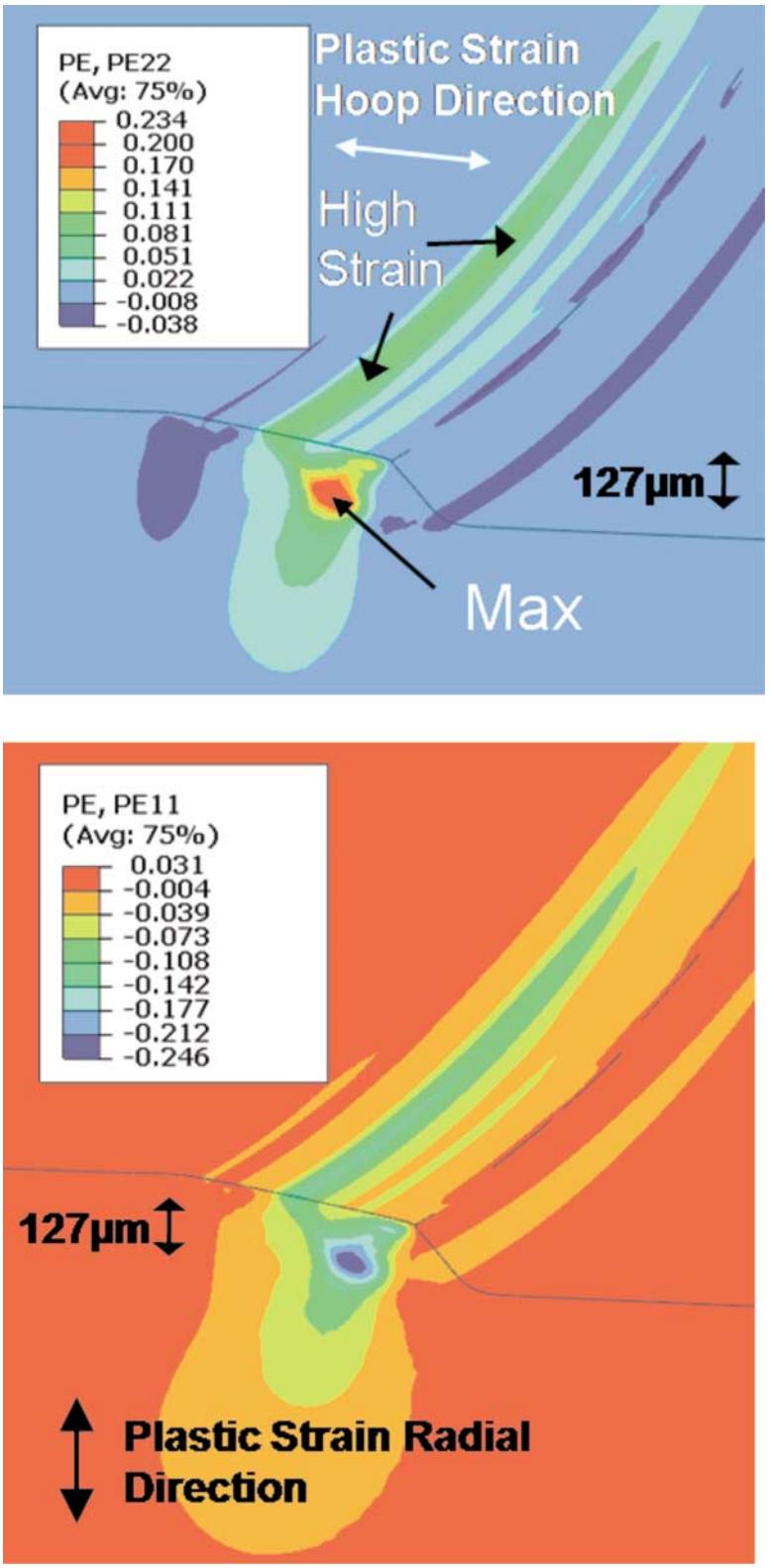

FIG. 16—*Hoop and radial plastic strains. Radial plastic strain is mostly compressive around edge of spall. Locations of large tensile hoop plastic strain are close to where cracks appear.*

blunt spall are not as severe as the sharper spall edge, but the fact that the stress gradients are similar helps show the dependency of spall shape in the finite element results.

Conclusions

This analysis represents a first attempt to capture the critical stresses and strains that develop in a spall edge during and after successive ball impacts. The validity of the finite element results is strengthened by

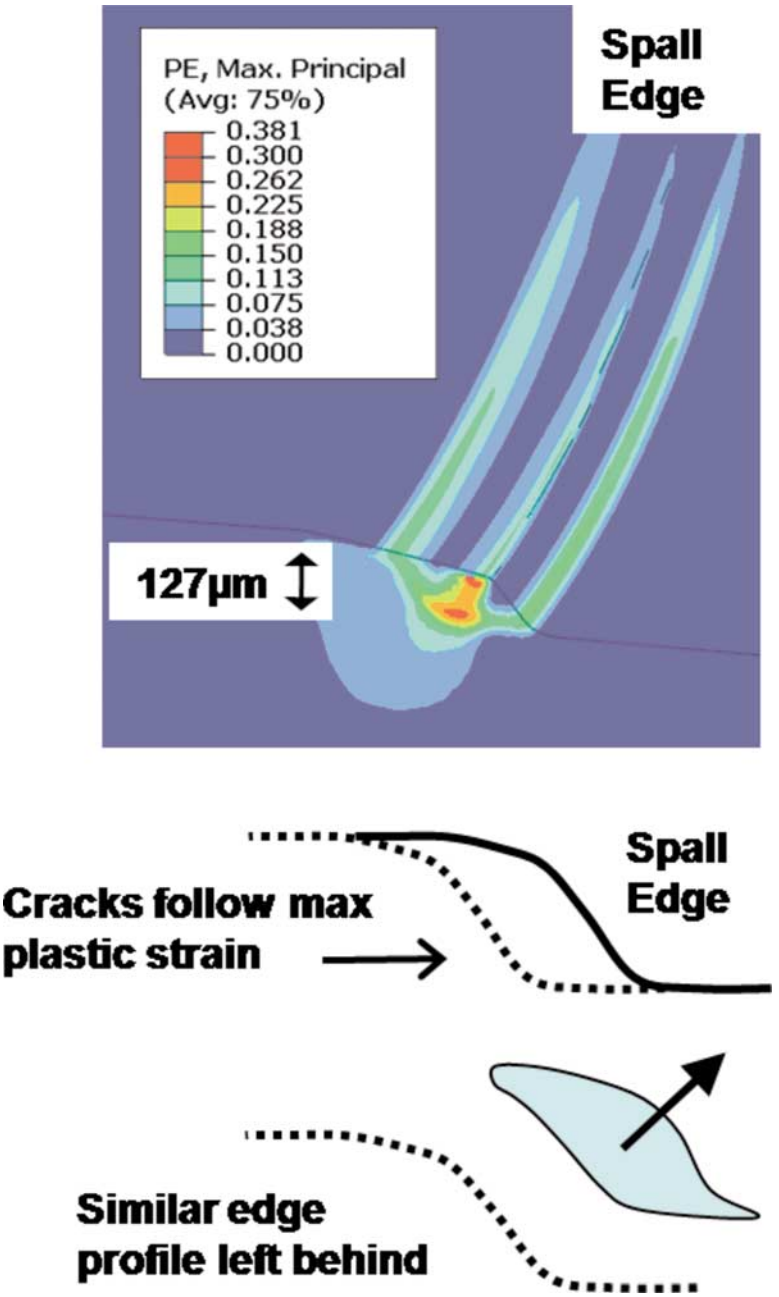

FIG. 17—*Maximum principal plastic strain.*

the locations and magnitudes of the residual stress profiles calculated from XRD techniques and the locations of cracks on the impacted spall edges observed in spall propagation experiments.

It is well understood that residual tensile stresses decrease the fatigue life of a material [4]. The finite element model determines residual hoop, radial, and hydrostatic tensile stresses to occur within an impacted spall edge at the same locations where fatigue cracks are observed in experiments. The computed residual compressive stresses below the trailing edge of the spall retard crack growth and keep material loss localized to the immediate surface as seen in experiments.

The distribution of plastic strain within the spall edge provides a likely path of crack growth which leads to the liberation of material fragments during spall propagation. This is supported by the observation that the spall edge shape remains consistent throughout propagation and closely matches the distribution of maximum principal plastic strain. Qualitative strain-life methodologies predict cracks to initiate in regions of high plastic strain. Cracks appear on spall edges where the finite element model predicts large plastic strain.

Future research will investigate how the impact between the ball and spall edge is affected by the

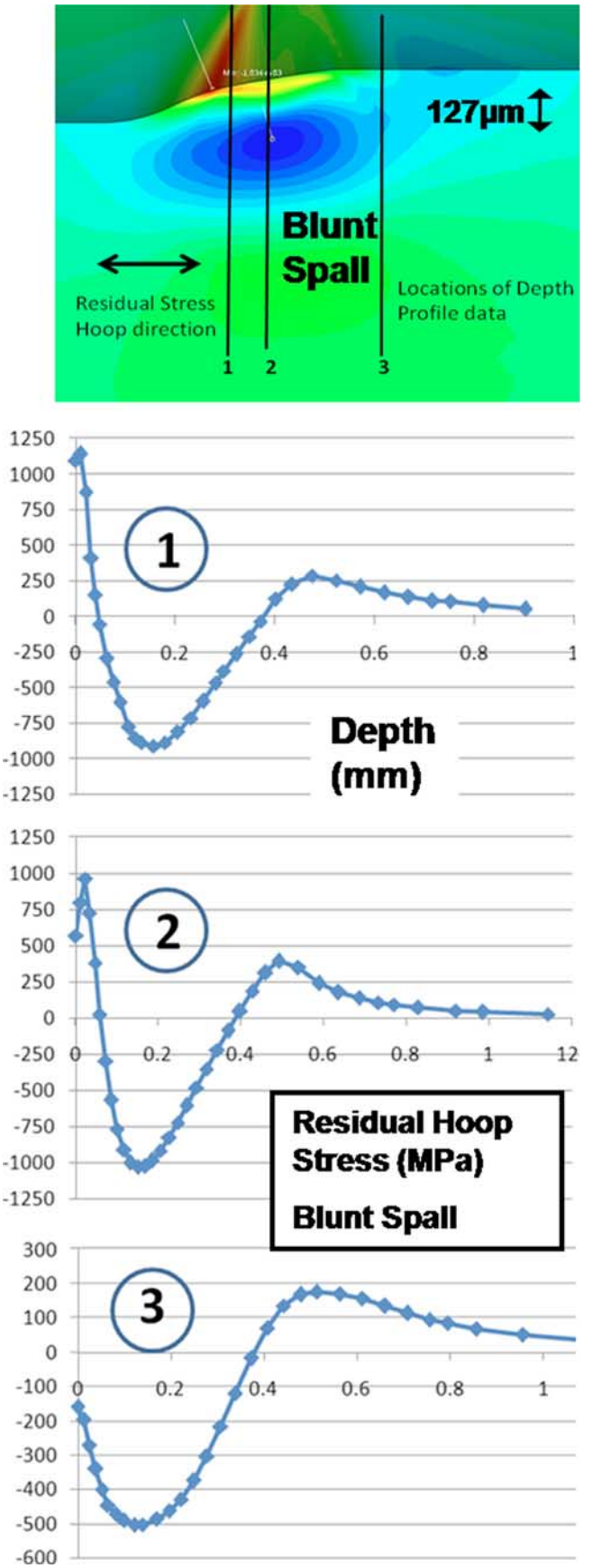

FIG. 18—*Residual hoop stresses for blunt spall similar to that of sharp spall.*

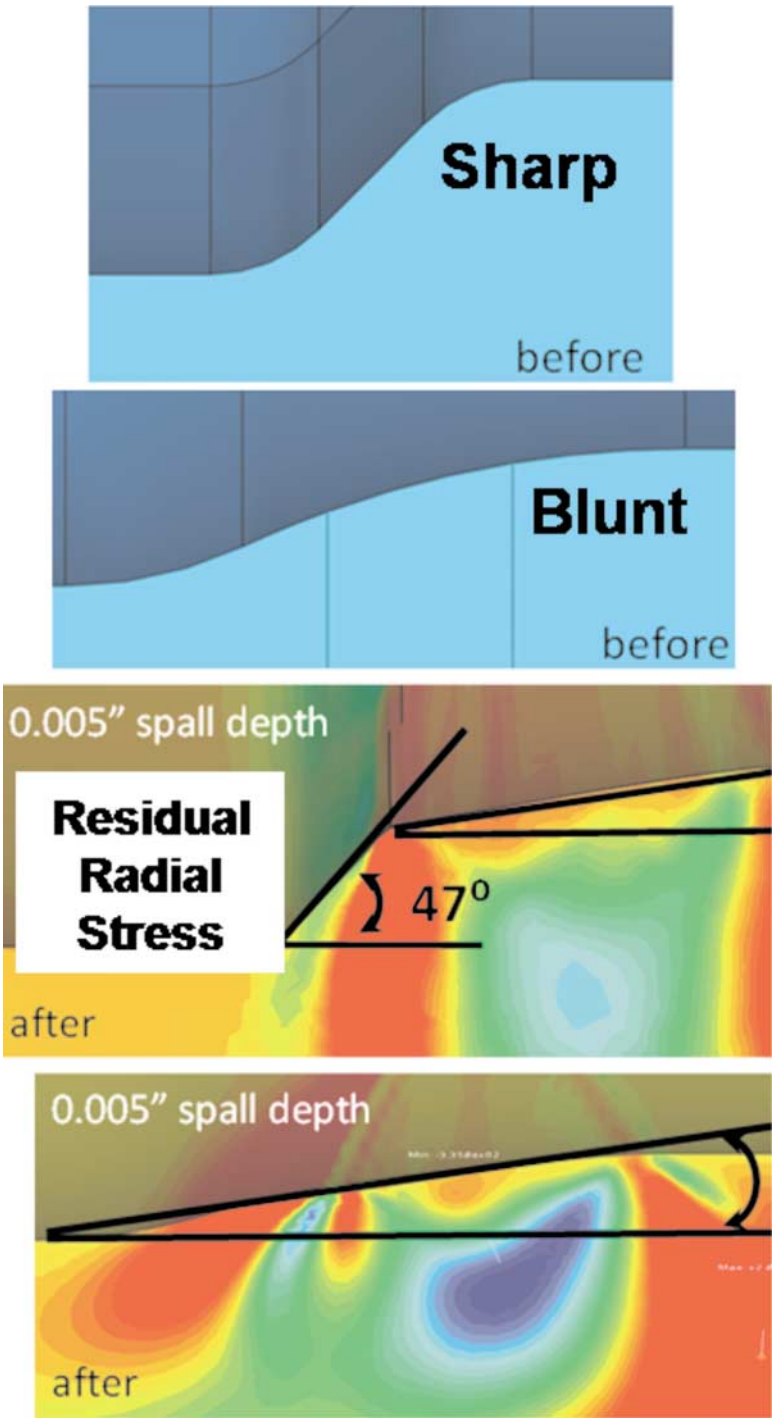

FIG. 19—*Before and after images of sharp and blunt spalls. Similar radial residual stresses are obtained.*

presence of the outer raceway and bearing cage. Changes in material properties due to microstructure decay are expected to occur in actual bearings, and this influence should be included. Future work will also explain why spall propagation rates differ between case and through-hardened bearing materials.

Acknowledgments

This work was supported by the Air Force Research Laboratory (AFRL), Wright Patterson Air Force Base, OH 45433, and the Timken Co., Canton, OH. The writers would like to thank Hitesh Trivedi of UES for taking profile measurements of the spall's trailing edges. Thanks also to Kevin Thompson of AFRL for all of the photographs of the bearing spalls and involvement in the spall propagation experiments. Sincere

appreciation is expressed to Mike Klecka and Dr. Ghatu Subhash for the compression tests of the M50 steel specimens. Special thanks to Dr. Liz Cooke, Dr. Bill Hannon, and Bob Wolfe of Timken Co. for their insight and contributions to this project.

References

[1] Miner, J. R., Dell, J., Galbato, A., and Ragen, M. A., "F-117-PW-100 Hybrid Bearing Ceramic Technology Insertion," *Trans. ASME J. Eng. Gas Turbines Power*, Vol. 118, 1996, pp. 434–442.

[2] Tanimoto, K., Kajihara, K., and Yanai, K., "Hybrid Ceramic Ball Bearings for Turbochargers," *SAE Paper No. 2000-01-1339*, 2000, pp. 1–14.

[3] Wang, L., Snidle, R. W., and Gu, L., "Rolling Contact Silicon Nitride Bearing Technology: A Review of Recent Research," *Wear*, Vol. 246, 2000, pp. 159–173.

[4] Sadeghi, F., Jalalahmadi, B., Slack, T. S., Raje, N., Arakere, N. K., "A Review of Rolling Contact Fatigue," *Trans. ASME, J. Tribol.*, Vol. 131, No. 4, 2009, 041403:1–15.

[5] Clarke, T. M., "The Role of Near Surface Inclusions in the Pitting of Gears," *ASLE Trans.*, Vol. 28, No. 1, 1984, pp. 111–116.

[6] Ringsberg, J. W., "Life Prediction of Rolling Contact Fatigue Crack Initiation," *Int. J. Fatigue*, Vol. 23, 2001, pp. 575–586.

[7] Lundberg, G. and Palmgren, A., "Dynamic Capacity of Rolling Bearings," *Acta Polytechnica*, Vol. 1, 1947, pp. 1–52.

[8] Zaretsky, E. V., "Comparison of Life Theories for Rolling Element Bearings," *Tribol. Trans.*, Vol. 39, No. 2, 1996, pp. 237–248.

[9] Kotzalas, M. and Harris, T. A., "Fatigue Failure Progression in Ball Bearings," *Trans. ASME*, Vol. 123, 2001, pp. 238–242.

[10] Ioannides, E. and Harris, T., "A New Fatigue Life Model for Rolling Bearings," *Trans ASME, J. Tribol.*, Vol. 107, 1985, pp. 367–378.

[11] Xu, G. and Sadeghi, F., "Spall Initiation and Propagation Due to Debris Denting," *Wear*, Vol. 201, 1996, pp. 106–116.

[12] Hoeprich, M. R., "Rolling Element Bearing Fatigue Damage Propagation," *Trans. ASME J. Tribol.*, Vol. 114, 1992, pp. 328–333.

[13] Rosado, L., Forster, N., and Thomson, K., "On the Rolling Contact Fatigue Life and Spall Propagation Characteristics of M50, M50 NiL and 52100 Bearing Materials: Part I—Experimental Results," *STLE Tribol. Trans.*, Vol. 53, 2010, 29–41.

[14] Arakere, N. K., Branch, N., Levesque, G., Svendsen, V., and Forster, N. H., "On the Rolling Contact Fatigue Life and Spall Propagation Characteristics of M50, M50 NiL and 52100 Bearing Materials: Part II—Stress Modeling," *STLE Tribol. Trans.*, Vol. 53, 2010, 42–51.

[15] Forster, N. H., Ogden, W. P., and Trivedi, H. K., "On the Rolling Contact Fatigue Life and Spall Propagation Characteristics of M50, M50 NiL and 52100 Bearing Materials: Part III—Metallurgical Examination," *STLE Tribol. Trans.*, Vol. 53, 2010, 52–59.

[16] Carpenter, "Hot Tensile Properties of Carpenter VIM VAR M50 Bearing Steel," www.cartech.com (Last accessed September 15, 2009).

[17] *ABAQUS, v6.8.2; Users Manual.* (2007), Dassault Systemes, ABAQUS software package.

[18] Suresh, S., *Fatigue of Materials*, 2nd ed., Cambridge University Press, New York, 2004.

[19] Howell, M. B., Rubin, C. A., and Hahn, G. T., "The Effect of Dent Size on the Pressure Distribution and Failure Location in Dry Point Frictionless Rolling Contacts," *Trans. ASME, J. Tribol.*, Vol. 126, 2004, pp. 413–421.